Supporting Information

One Step in situ Synthesis of Core-shell Structured Cr_2O_3:P@Fibrous-Phosphorus Hybrid Composites with Highly Efficient Full-spectrum-response Photocatalytic Activities

*Hongpeng Zhou[a], Shixin Xu[b], Dingke Zhang[c], Shijian Chen[a] * and Junkai Deng[b] **

[a]School of Physics, Chongqing University, Chongqing, 401331, China

[b]State Key Laboratory for Mechanical Behavior of Materials, Xi'an Jiaotong University, Xi'an, 710049, China

[c]College of Physics and Electronic Engineering, Chongqing Normal University, Chongqing, 401331, China.

*Corresponding author
E-mail addresses: sjchen@cqu.edu.cn (S. Chen), junkai.deng@mail.xjtu.edu.cn (J. Deng).

1. Supplementary figures

2. Theoretical calculations

3. Heterojuction band alignment

4. Reference

1. Supplementary figure

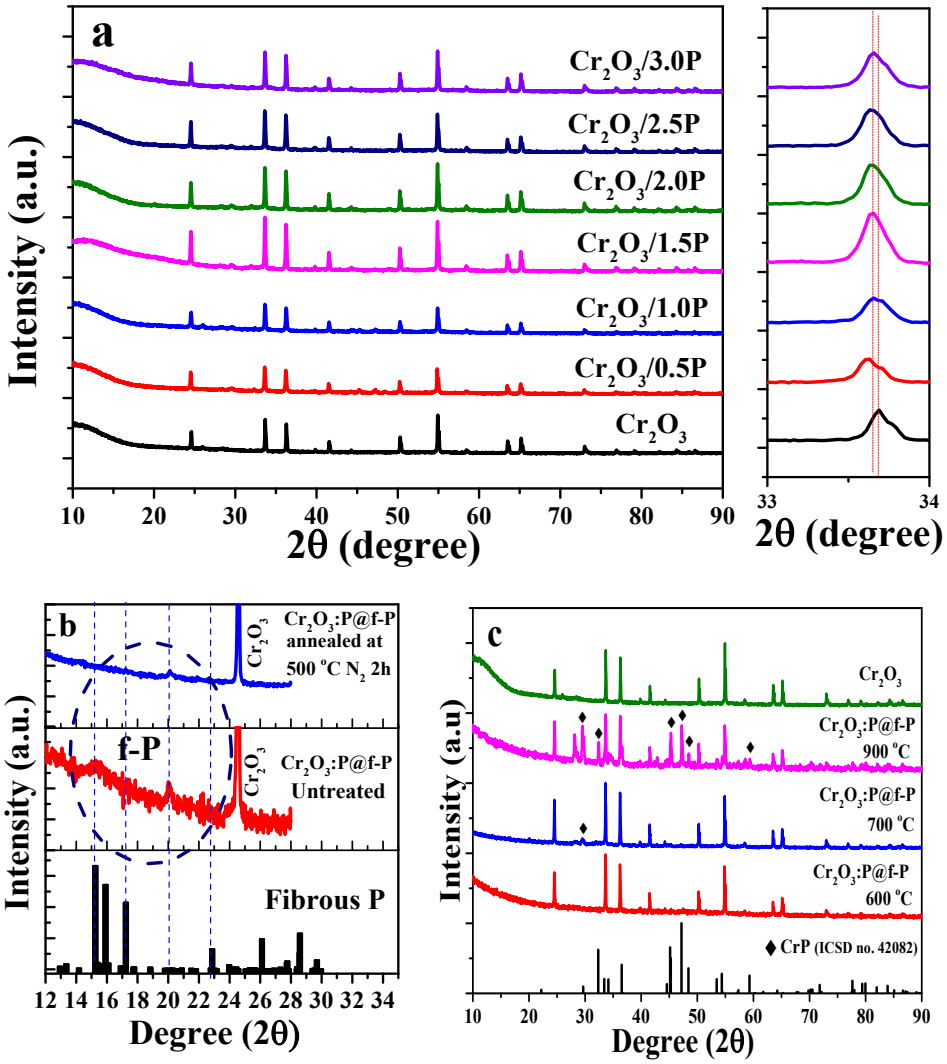

Figure S1 XRD patterns of (a) Cr_2O_3:P@f-P with different P content fired at 700 °C; (b) comparison of XRD patterns for Cr_2O_3:P@f-P (m=2.5) and Cr_2O_3:P@f-P (m=2.5) annealed in N_2 for 2 h; (c) XRD patterns of Cr_2O_3:P@f-P (m=2.5) calcined at 600 °C, 700 °C and 900 °C.

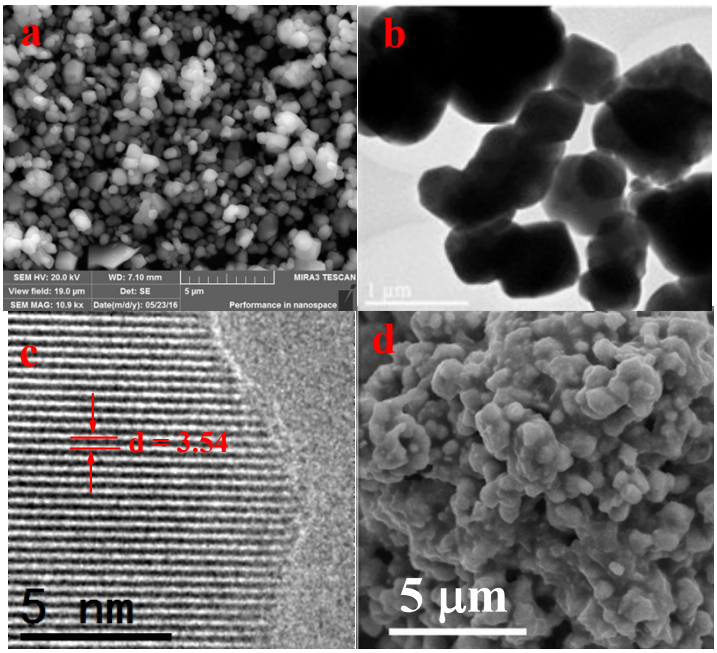

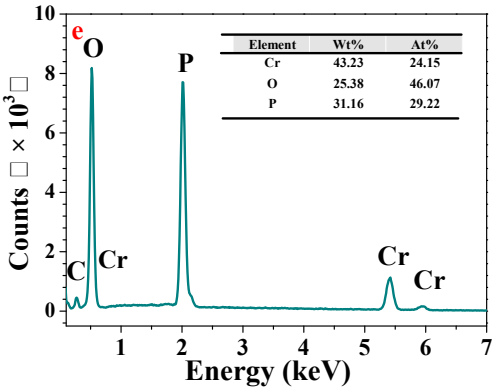

Figure S2 (a-c) SEM, TEM and HRTEM images of pure Cr_2O_3; (d-e) FESEM image and corresponding EDS spectra of Cr_2O_3:P@f-P (m=2.5).

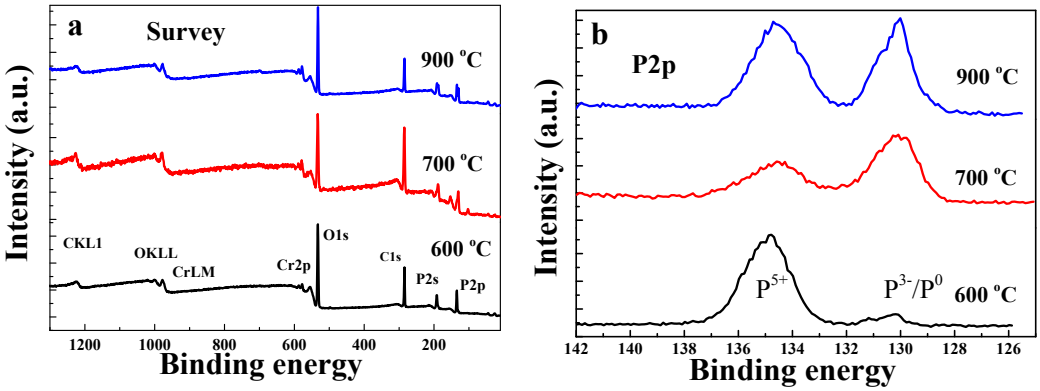

Figure S3 (a) survey XPS spectra of Cr_2O_3:P@f-P (m=2.5) prepared at different temperature; (b)The high resolution P2p XPS spectra of Cr_2O_3:P@f-P (m=2.5) calcined at 600 °C, 700 °C and 900 °C, respectively.

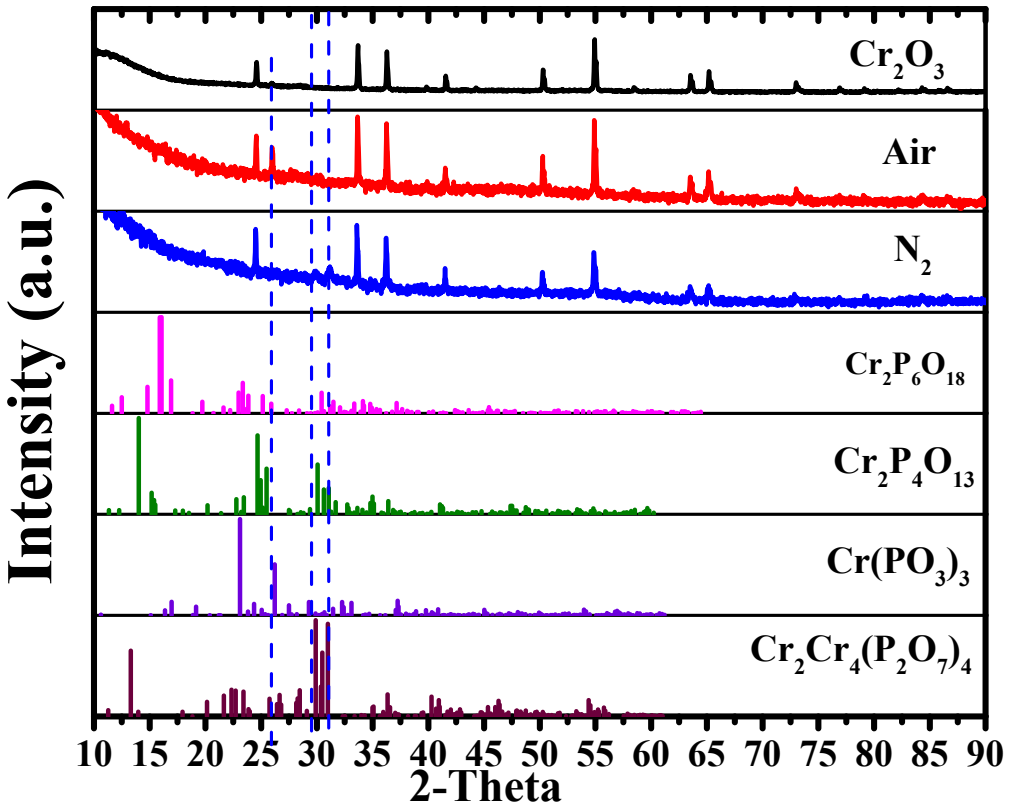

Figure S4 the XRD pattern of possible phosphate impurities for Cr_2O_3:P@f-P (m=2.5) after TGA measurements in the N_2 and air atmosphere.

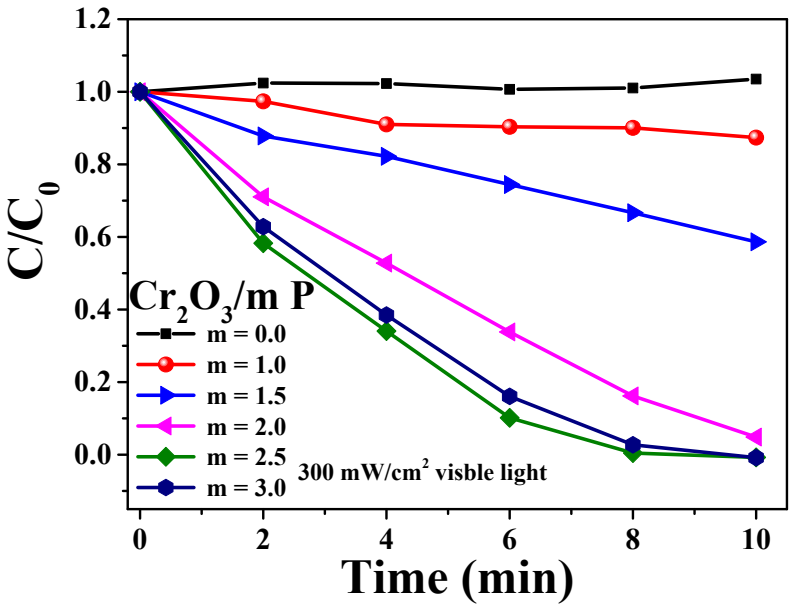

Figure S5 Photocatalytic degradation activities of the Cr_2O_3:P@f-P composites prepared with different molar ratio (m) of P to Cr_2O_3 under visible light irradiation (pH = 7).

Photocatalysts	Target pollutants	Light source	Light density (mw/cm^2)	Catalyst dosage (mg)	Pollutants concentration (mg/L) / Dosage (ml)	Activity（min）	Degradation efficiency（%）	Ref (year)
Cr_2O_3:P@f-P	MO	300 W Xe lamp, > 800 nm	95	20	10 / 100	300	100 %	This work
WS_2	MO	5 W NIR LED, (800-900 nm)	95	50	20 / 50	300	80 %	[1] (2015)
α-$NaYF_4$:Yb, Tm/TiO_2/rGO	MO	2 W LED laser, 980 nm	-	65	15 / 5	720	70 %	[2] (2016)
α-$NaYF_4$:Yb, Tm/TiO_2	MO	1 W LED laser, 980 nm	-	5	20 / 0.5	1500	70 %	[3] (2013)
α-$NaYF_4$:Yb, Tm/ZnO	RhB	2 W LED laser, 980 nm	2000	0.5	20 / 0.5	1800	55%	[4] (2013)
Bi_2WO_4/TiO_2	MO	250 W NIR lamp, > 760 nm	-	20	20 / 20	120	74 %	[5] (2013)
TiO_2/WO_{3-x}	MB	200 W NIR lamp, > 800	-	100	50 / 50	250	30 %	[6] (2016)
CQDS/H-TiO_2	MO	250 W NIR lamp > 760 nm	-	20	20 / 20	120	32%	[7] (2015)
$Cu_2(OH)PO_4$	2,4-DCP	> 800 nm	-	-	20 / -	360	90 %	[8] (2013)
Er^{3+}/Yb^{3+}-(CaF_2 @TiO_2)	MO	500 W Xe lamp, 720-1100 nm	-	50	10 / 50	720	30 %	[9] (2013)
Cs_xWO_3	MB	200 W NIR lamp, >800 nm	42.7	100	50 / 50	360	37%	[10] (2016)

Table S1 Comparison of NIR photocatalytic performance for Cr_2O_3:P@f-P hybrid composites with other NIR photocatalysts

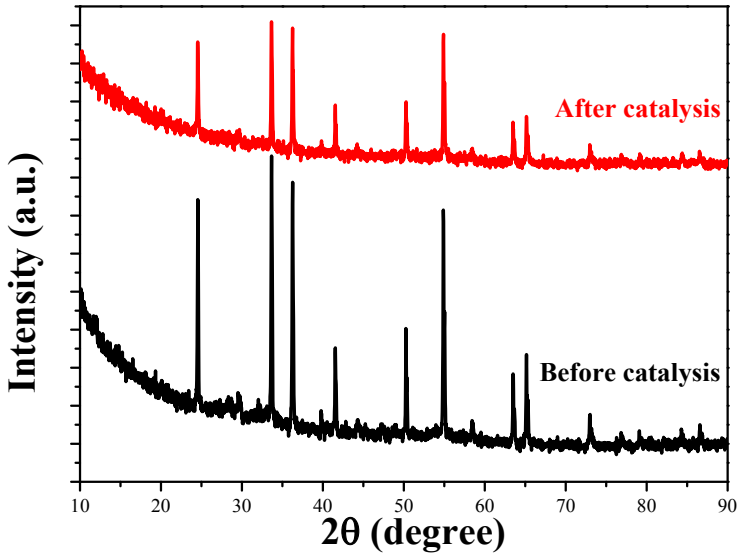

Figure S6 The XRD patterns of core-shell structured Cr_2O_3:P@f-P (m=2.5) hybrid composites before and after photodegradation process.

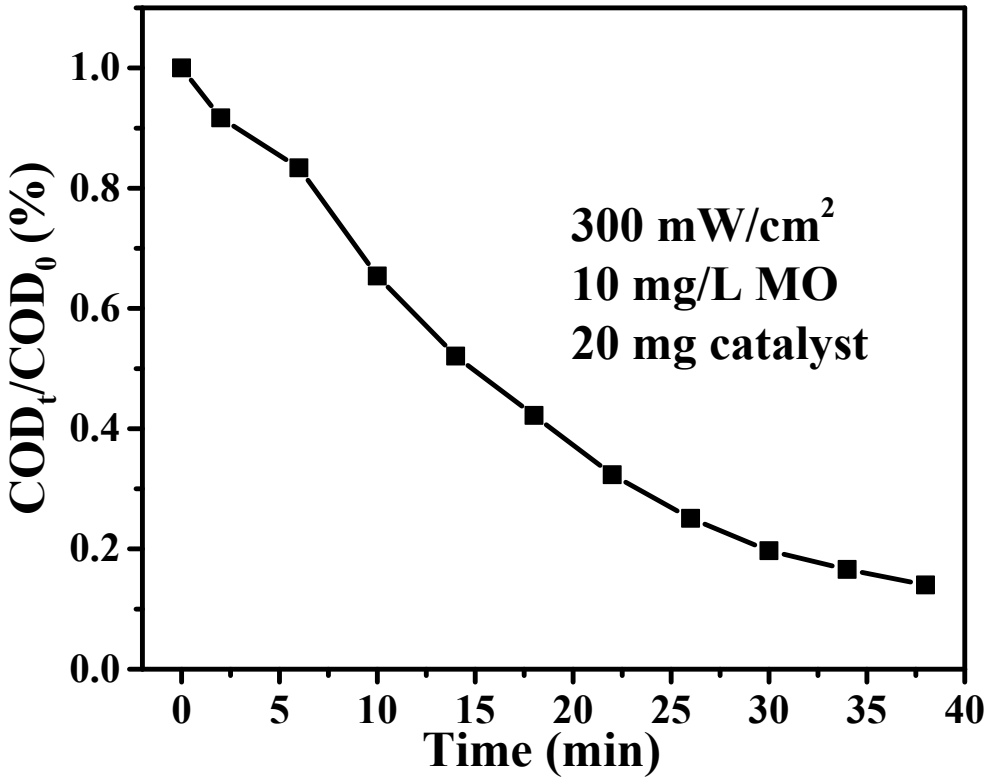

Figure S7 the COD removal efficiency of MO under 300 mW/cm^2 light density

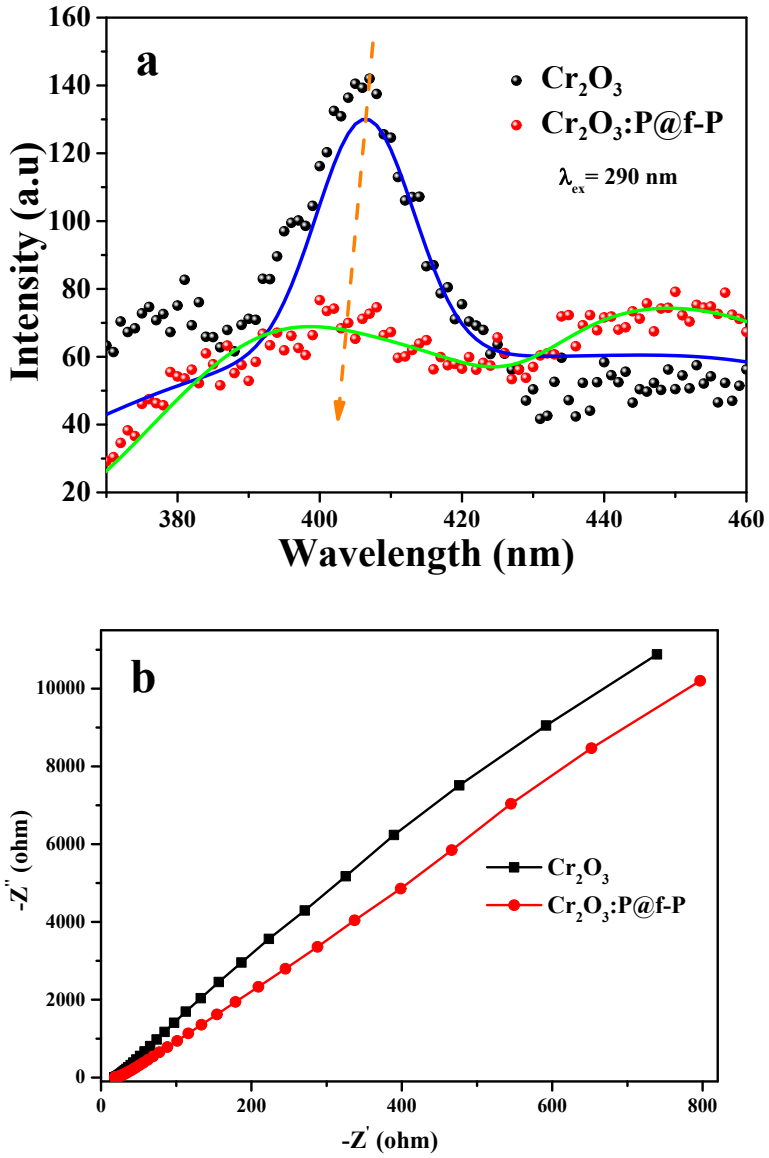

Figure S8 (a) The photoluminescence spectra (PL) of pure Cr_2O_3 and core-shell structured Cr_2O_3:P@f-P (m=2.5) hybrid composites upon 290 nm light excitation; **(b)** EIS Nyquist plots of pure Cr_2O_3 and core-shell structured Cr_2O_3:P@f-P (m=2.5) hybrid composites in the 0.2M Na_2SO_4 solution.

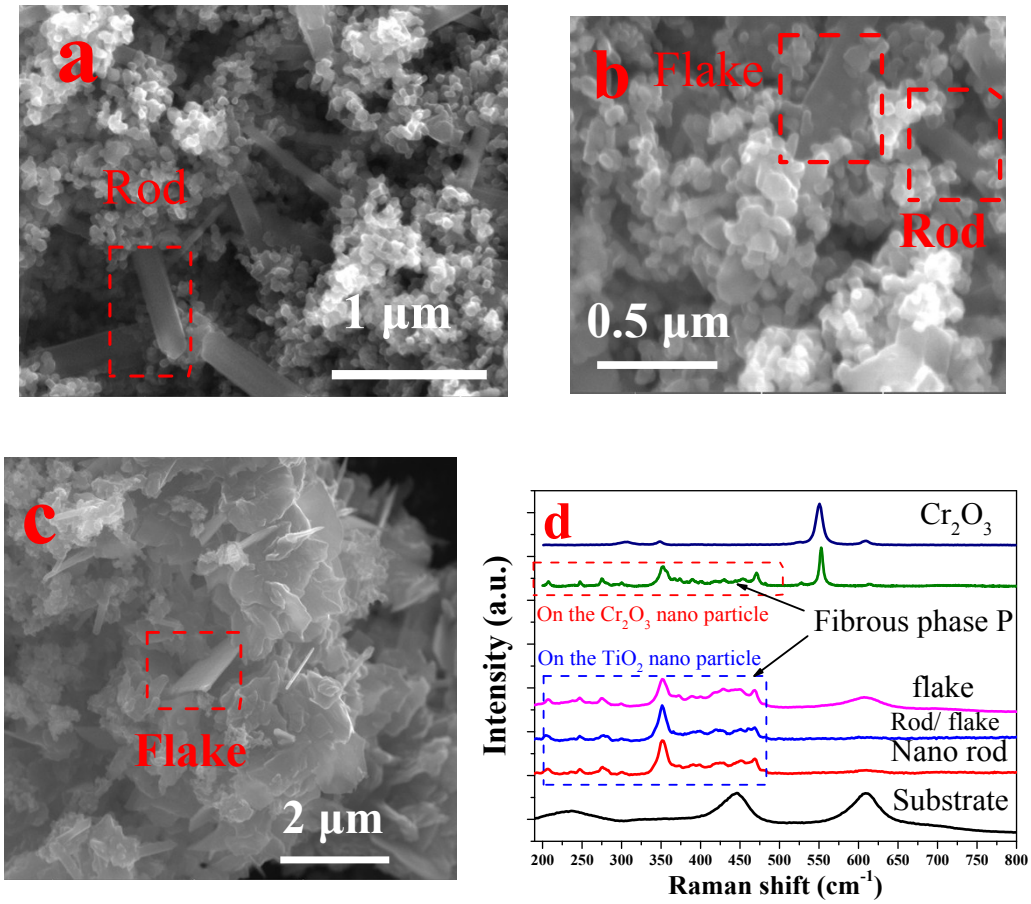

Figure S9 (a-c) The SEM image of nano rod, nano rod/ flake and flake morphology fibrous phase P on the surface of TiO_2; (d) The comparison of Raman spectra of fibrous phase P grown on Cr_2O_3 and TiO_2.

Figure S9(a-c) shows the SEM images of fibrous phase P grown on Cr_2O_3 and TiO_2, respectively. The results imply fibrous phase P can be different morphologies such as nanorod, nanoflake synthesized on different particles via adjusting experimental conditions. The Raman spectra for all the samples can be well indexed to fibrous phase P.

2. Theoretical calculations

The theoretical calculations were carried out with the Vienna ab initio simulation package (VASP) based on density-functional theory (DFT) using projector augmented wave (PAW) potentials. [11] The electron exchange correlation interaction was described by Generalized Gradient Approximation (GGA) with the Perdew-Burke-Ernzerhof (PBE) exchange correlation functional.[12] The LSDA+U (i.e., PBE+U) method was performed for antiferromagnetic (AFM) Cr_2O_3, with a small effective on-site Coulomb energy U_{eff} of 3.3 eV for the chromium d electrons. The plane wave kinetic energy cutoff was set at 520 eV, and a 9 × 9 × 9 uniform Monkhorst-Pack k-grid was used for all calculated cells. Periodic boundary conditions were employed in all DFT calculations. All atoms were fully relaxed until the Helmann − Feynman forces were less than 0.001 eV/Å.

Table S2: Formation energy of P impurities in Cr_2O_3 crystal to form $Cr_2O_{3-x}P_x$.

Model	**1P atom**	**2P atom-1**	**2P atom-2**	**3P atom-1**	**3P atom-2**
Concentration (x)	0.0625	0.125	0.125	0.1875	0.1875
E_{form} (eV)	-3.236	-2.922	-2.878	-2.326	-2.609

In order to investigate the P doped Cr_2O_3, we created a supercell including 80 atoms (32 Cr atom and 48 O atom) of 16 unit cells. We then introduced 1, 2 or 3 P

atoms to replace the O atoms randomly distributed. Five models involves different numbers of P atoms are shown in **Figure S10b**. The formation energy (E_{form}) of impurity P in Cr_2O_3 was computed by formula shown as following:

$$E_{form} = (E_{Cr_2O_{3-x}P_x} + x \cdot E_O) - (E_{Cr_2O_3} + x \cdot E_P) \quad (1)$$

Here, $E_{Cr_2O_3}$ is the energy per unit cell for pure Cr_2O_3; $E_{Cr_2O_{3-x}P_x}$ is the energy per unit cell for P doped Cr_2O_3; *x* represents the concentration of P defects in one unit cell of Cr_2O_3 (to form $Cr_2O_{3-x}P_x$). E_O and E_P denote the energy of single O atom and single P atom for their ground states, respectively. This equation describes the formation energy of P atoms doped in Cr_2O_3 to replace O atoms. The calculated formation energies are in between -2.33 per unit and -3.24 eV per unit as shown in **Table S2**. Although they are obviously dependent on the concentration and geometrical configuration of P impurities, the negative values suggest that P atoms are feasible to dope into the Cr_2O_3.

Figure S10a shows that doping one P into Cr_2O_3 supercell will lead to the defective bands within the bandgap due to the hybrid of Cr 3p3d4s, O 2p and P 3p. The curves of band structure presented in Figure S10b demonstrate that the P impurities contribute the "defective bands" (plotted as red lines) within the band gap. Compared with different models shown in Figure S10b (1 to 5), the DOS curves reveals that the defect levels are highly dependent on the concentration and geometrical configurations of doped P atoms. With the increase of the doping content, the defective bands with different energy level form within the band gap. It guarantees the light absorption extending to NIR region.

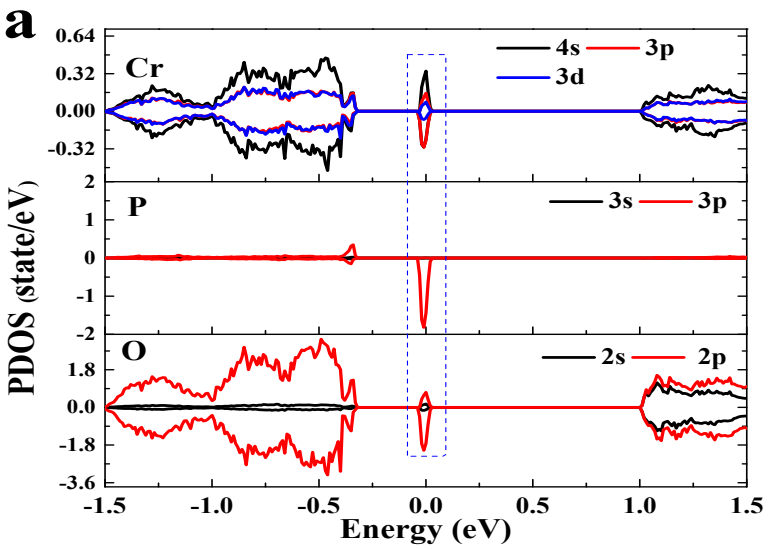
a
Cr
4s
3p
3d
P
3s
3p
O
2s
2p
PDOS (state/eV)
Energy (eV)

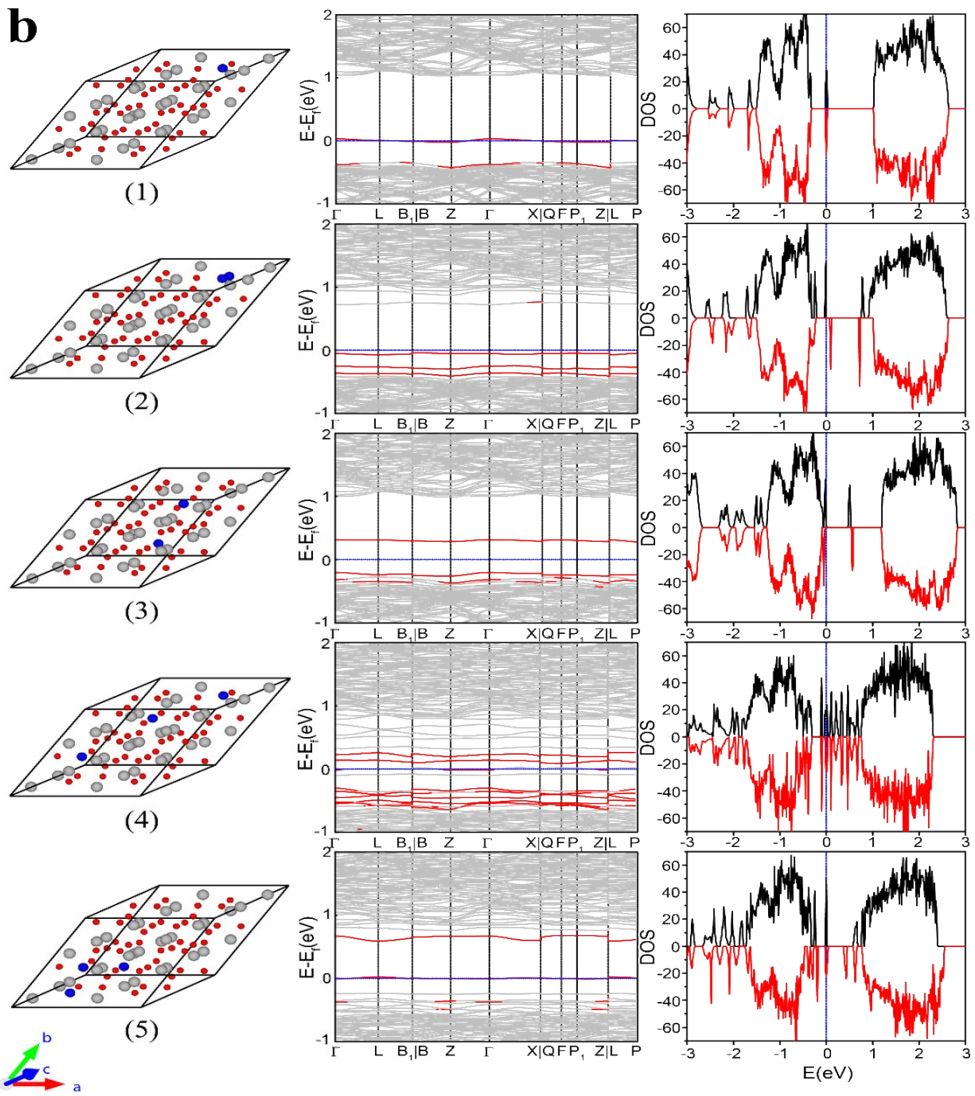
b
(1)
(2)
(3)
(4)
(5)
E-E_f(eV)
Γ L B_1|B Z Γ X|Q F P_1 Z|L P
DOS
E(eV)
b
c
a

Figure S10 (a) The calculated density of partial state (PDOS) of Cr_2O_3:P using the PBE+U method; (b) The structure details (Color represents: red, O; grey Cr, blue P;), calculated electronic band structure and density of state (DOS) using the PBE+U method at different concentration P doing Cr_2O_3. (1): one P atom randomly substitution for O sites; (2) and (3): two P atom randomly substitution for O sites; (4) and (5): three P atom randomly substitution for O sites, respectively.

3. Heterojuction band alignment

The conductive band (CB) and valence band (VB) positions of Cr_2O_3:P can be estimated by Mulliken electronegativity theory,[13] which values at the point of zero charge can be calculated by following formula:

$$E_{CB} = \chi - E + 0.5E_g$$
$$E_{VB} = E_{CB} + E_g \quad (2)$$

Where E_{CB} and E_{VB} are the potential of conduction band and valance band, respectively. χ is the geometric mean of electronegativity of the component atoms, E_c (4.5 eV) is the scaling factor between the hydrogen electrode scale (NHE) and absolute vacuum scale (AVS). Here, by using χ= 5.68 and E_g = 2.9 eV, the E_{CB} and E_{VB} were calculated to be -0.27 V and 2.63 V (vs. NHE, pH = 0), respectively. Here the obtained band gap (E_g) of Cr_2O_3:P is 2.9 eV (**Figure 3**). And the CB potential of fibrous is -0.9 V vs. NHE (pH = 0) according to literature. According to the above values, we draw the schematic diagram of band structures for Cr_2O_3:P and fibrous P before contact, as shown in **Figure S11**. As we have known from the calculated band structures, the valence band is close to its Fermi level for p-type semiconductor.[14] Thus, the Fermi level of Cr_2O_3:P is more positive than fibrous P. After Cr_2O_3:P and f-P contact, the band position of Cr_2O_3:P will shift upward along with its Fermi level while those of fibrous P will shift downward along until established the equilibrium of Fermi level between two semiconductors. Finally, there will be a built-in potential between the core-shell contact interfaces, which can dramatically enhance the

separation of photogenerated electron and holes and then improve photocatalytic performance.

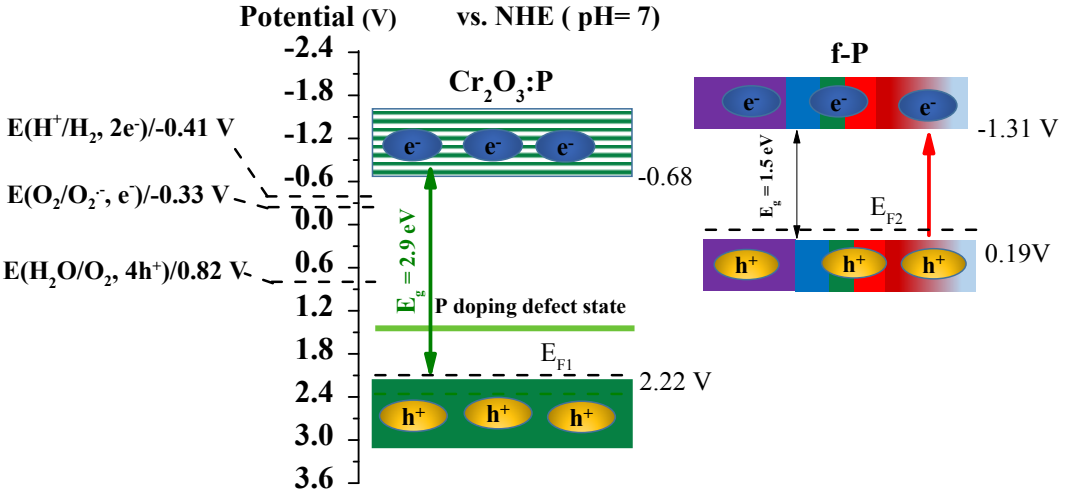

Figure S11 Schematic diagram of band structures for Cr_2O_3:P and fibrous P before contact.

4. Reference

1. Y. Sang, Z. Zhao, M. Zhao, P. Hao, Y. Leng and H. Liu, *Adv. Mater.*, 2015, **27**, 363.
2. W. J. Wang, Y. C. Li, Z. W. Kang, F. Wang and J. C. Yu, *Appl. Catal., B*, 2016, **182**, 184.
3. D. X. Xu, Z. W. Lian, M. L. Fu, B. L. Yuan, J. W. Shi and H. J. Cui, *Appl. Catal., B*, 2013, **142**, 377.
4. X. Y. Guo, W. Y. Song, C. F. Chen, W. H. Di and W. P. Qin, *Phys. Chem. Chem. Phys.*, 2013, **15**, 14681.
5. J. Tian, Y. Sang, G. Yu, H. Jiang, X. Mu and H. Liu, *Adv. Mater.*, 2013, **25**, 5075.
6. M. Yan, G. L. Li, C. S. Guo, W. Guo, D. D. Ding, S. H Zhang and S. Q. Liu, Nanoscale, 2016, 17828.
7. J. Tian, Y. Leng, Z. Zhao, Y. Xia, Y. Sang, P. Hao, J. Zhan, M. Li and H. Liu, *Nano Energy*, 2015, **11**, 419.
8. G. Wang, B. B. Huang, X. C. Ma, Z. Y. Wang, X. Y. Qin, X. Y. Zhang, Y. Dai and M. H. Whangbo, *Angew. Chem. Int. Ed.*, 2013, **52**, 4810.
9. S. Q. Huang, L. Gu, C. Miao, Z. Y. Lou, N. W. Zhu, H. P. Yuan and A. D. Shan, *J. Mater. Chem. A*, 2013, **1**, 7874.
10. G. L. Li, C. S. Guo, M. Yan and S. Q. Liu, *Appl. Catal., B*, 2016, **183**, 142.

11. G. Kresse and J. Furthmuller, *Comput. Mater. Sci.*, 1996, **6**, 15.
12. J. P. Perdew, K. Burke and M. Ernzerhof, *Phys. Rev. Lett.*, 1997, **78**, 1396.
13. Y. Xu and M. A. A. Schoonen, *Amer. Mineral.*, 2000, **85**, 543-556.
14. D. Lang, F. Y. Cheng and Q. J. Xiang, *Catal. Sci. Technol.*, 2016, **6**, 6207.